Double Pion Photoproduction on Deuteron(I. Nuclear Physics)

著者	Hirose Kentarou, Ejima Mitsuhiko, Fujibayashi Takeji, Fujii Yuu, Futatsukawa Kenta, Hashimoto Osamu, Ishikawa Takatsugu, Kameoka Satoru, Kanda Hiroki, Kato Fumiaki, Kinoshita Sari, Kinoshita Tadashi, Kon Takashi, Konno Osamu, Maeda Kazushige, Matsumura Akihiko, Miura Yusuke, Miyahara Fusashi, Miyase Haruhisa, Nakabayashi Tadashi, Nakamura Satoshi Nue, Nomura Hiroshi, Ohtani Atsushi, Okayasu Yuichi, Oyamada Masamichi, Sasaki Atsushi, Shimizu Hajime, Tsukada Kyo, Takahashi Toshiyuki, Tamae Tadaaki, Tamura Hirokazu, Terasawa Tatsuo, Tsubota Hiroaki, Uchida Daisuke, Ukai Mifuyu, Yamauchi Hirokazu, Yamazaki Hirohito, Yawata Keisuke, Wakamatsu Masaki, Watanabe Takaomi
journal or publication title	核理研研究報告
volume	39
page range	7-20
year	2007-03
URL	http://hdl.handle.net/10097/40385

(LNS Experiment : #2464, #2551)

Double Pion Photoproduction on Deuteron

K. Hirose[1,*], M. Ejima[1], T. Fujibayashi[1], Y. Fujii[1], K. Futatsukawa[1], O. Hashimoto[1], T. Ishikawa[2], S. Kameoka[1], H. Kanda[1], F. Kato[1], S. Kinoshita[1], T. Kinoshita[2], T. Kon[1], O. Konno[4], K. Maeda[1], A. Matsumura[1], Y. Miura[1], F. Miyahara[2], H. Miyase[1], T. Nakabayashi[2], S.N. Nakamura[1], H. Nomura[1], A. Ohtani[1], Y. Okayasu[1], M. Oyamada[1], A. Sasaki[3], H. Shimizu[2], K. Tsukada[1], T. Takahashi[1,†], T. Tamae[2], H. Tamura[1], T. Terasawa[2], H. Tsubota[1], D. Uchida[1], M. Ukai[1,§], H. Yamauchi[1], H. Yamazaki[2], K. Yawata[1], M. Wakamatsu[1], T. Watanabe[1,‡]

[1] *Department of Physics, Tohoku University, Sendai, 980-8578*
[2] *Laboratory of Nuclear Science, Tohoku University, Sendai, 982-0826*
[3] *Department of Electrical and Electronic Engineering, Akita University, Akita, 010-8502*
[4] *Department of Electrical Engineering, Ichinoseki National College of Technology, Ichinoseki, 021-8511*

Exclusive cross sections for double-pion photoproductions on proton and deuteron were measured in an energy range from 0.8 to 1.1 GeV using tagged photons at Laboratory of Nuclear Science, Tohoku University. We employed the Neutral Kaon Spectrometer (NKS) to detect two pions in the final state, and deduced the cross section for the $\pi^+\pi^-$ photoproduction on the "free" and "bound" proton. We have discriminated between the quasi-free and non-quasi-free process applying the kinematical cut on the missing momentum. We found that the total cross section for the γ"p"$\rightarrow p\pi^+\pi^-$ reaction was about 60% of that for the "free" proton, and this is consistent with the previously obtained data. The one of the dominant part of the non-quasi-free process was found to be the double Δ production. Its cross section is smaller than the previous investigations.

§1. Introduction

In the pion photoproductions above the second resonance region, the doublepion emissions in the final state become important with increasing the photon energy. Recently, data for the multi-particle

*Present address : Laboratory of Nuclear Science, Tohoku University, Sendai, 982-0826
†Present address : Institute of Particle and Nuclear Studies, High Energy Accelerator Organization (KEK), Tukuba, 305-0801
§Present address : Cyclotron and Radioisotope Center, Tohoku University, Sendai, 980-8678
‡Present address : Gifu University, Gifu, 501-1193

detection are carried out using not only bubble chambers [1-4] but also large acceptance spectrometers using tagged photon beams.

Since large acceptance photon spectrometers became available, the compilation of the exclusive pion photoproduction data have proceeded including the neutral pion photoproductions [5, 6]. Measurements of double pion phtoproduction using a deuterium target have been also done. The deuteron is often used as a neutron target under the assumption of the quasi-free (QF) process.

One of the result from these studies is that a large isospin dependence is not found in double pion photoproduction on the nucleon. This is thought to be valid considering that the photoabsorption data approximately satisfy the following relation [7-9],

$$\sigma(\gamma d \rightarrow X) \approx 2\,\sigma(\gamma p \rightarrow X). \qquad (1)$$

In the case of nuclear targets, the non quasi-free (NQF) process caused by the meson exchange current, the delta current and the final state interaction must be exclusively identified to select the QF channel. The contribution of the NQF process was studied in the $\gamma d \rightarrow pn\pi^+\pi^-$ reaction [10]. The result of this study is that the total cross section for $\pi^+\pi^-$ photoproduction on the "bound" proton is the same as that on the "free" proton within the statistical uncertainties, but the contribution of the NQF process is not negligible.

There are also data on the total cross section for the $\gamma n \rightarrow n\pi^+\pi^-$ reaction which were measured using the deuterium bubble chamber [3, 4]. The comparison between the total cross section for $\pi^+\pi^-$ photoproduction on the "bound" proton and that on the "bound" neutron has been done. Consequently, it is found that these values are the same within the statistical uncertainties, but they are smaller than that of "free" proton,

$$\sigma(\text{"}p\text{"} \rightarrow p\pi^+\pi^-) \approx \sigma(\gamma\,\text{"}n\text{"} \rightarrow n\pi^+\pi^-) < \sigma(\gamma p \rightarrow p\pi^+\pi^-), \qquad (2)$$

where "p" and "n" denote the "bound" proton and "bound" neutron, respectively. If the cross sections for the "bound" nucleon are the same as those for the "free" nucleon and there is a large contribution of the NQF process, this seems to contradict the result of the photoabsorption data (Eq. (1)).

The NQF process has not been studied in detail. Many body effects seem to appear, even though the deuteron is the simplest nuclei. We have measured double pion photoproduction on the proton and deuteron in order to investigate the NQF process in detail. The aims of this study are :

- To measure the total cross sections for $\pi^+\pi^-$ photoproduction on the "free" and "bound" proton.
- To investigate the contribution of the NQF process and $\Delta^{++}\Delta^-$ production in the $\gamma d \rightarrow pn\pi^+\pi^-$ reaction.

In this article, we describe the results of the double pion photoproduction on the proton and the deuteron to study the contributions of the NQF process.

§2. Experimental Procedure

The experiments were carried out using an internal photon tagging system and a magnetic spectrometer at Laboratory of Nuclear Science, Tohoku University.

2.1 Tagged photon beam

Electrons from the linear accelerator were injected into the Stretcher-Booster (STB) ring and accelerated up to 1.2 GeV. Bremsstrahlung photons were produced by the internal photon tagging system (STB-Tagger) [11]. It consists of a bremsstrahlung radiator, a bending magnet and a tagging hodoscope. A carbon fiber of 11 μmϕ was used for the radiator. It was inserted into the electron orbit by synchronizing the storage-phase of the STB ring. The momenta of the recoil electrons were analyzed in the magnetic field of the bending magnet of the STB ring. The tagging hodoscope consists of 48 finger counters and 12 backup counters. It covers the photon energy range from 0.8 to 1.1 GeV. The energy span of each finger counter was about 6 MeV. The tagging rate was 2 $\sim$ 3 MHz, and the tagging efficiency was 74 $\sim$ 83% in the whole tagging range. The photon beam impinged on the target through a lead collimator, 300-mm long and 10 mm in diameter, placed 3.8 m downstream of the bremsstrahlung radiator.

2.2 Target

A cryogenic system was used for liquid hydrogen and deuterium targets. The target container was a cylinder of 50 mmϕ and 30-mm length. It was located in the center of the spectrometer with its axis parallel to the beam line.

The cylinder was made of 1-mm thick aluminum frame with windows of 75-μm thick Upilex-S film [12] adhered on the both ends. A CFRP (carbon fiber reinforced plastic) chamber was employed for the vacuum insulation around the target. We also provided a beam window with the vacuum chamber.

The pressure and temperature of the target were monitored throughout the experiment. The temperature was automatically controlled and kept at 14.5 K and 19.1K, which correspond to the thickness of 254 mg/cm^2 and 571 mg/cm^2 for the hydrogen and deuterium target, respectively.

2.3 Spectrometer

The Neutral Kaon Spectrometer (NKS) was used for the detection of charged particles. It consists of two sets of drift chambers in the magnetic field, inner and outer hodoscopes, and electron veto counters.

2.3.1 Analyzer magnet

The dipole magnet had a 60-cm pole gap and a 107 cm ϕ circular pole face with a nominal field strength of 0.5 T. The distribution of the magnetic field was calculated by the TOSCA code [13] and scaled to the value measured at the center of the magnet. The non-uniformity was taken into account in the off-line data analysis.

2.3.2 Hodoscopes

Two sets of scintillation hodoscopes, inner (IH) and outer hodoscope (OH), were employed to give triggering signals to the online data acquisition system and to measure the time-of-flight (TOF) of charged particles. Each IH was made of six plastic scintillator elements of 20 ~ 25-mm width, 120-mm height and 5-mm thickness. As shown in Fig.1, they were located 60 mm away from the pole axis and surround the target. Since IHs were within the magnetic field, optical-fiber bundles were used to guide scintillation photons to photo-multiplier tubes (PMTs) placed away from the magnetic field. The OHs were made of 34 plastic scintillator elements of 130 ~ 170-mm width, 600-mm length and 10-mm

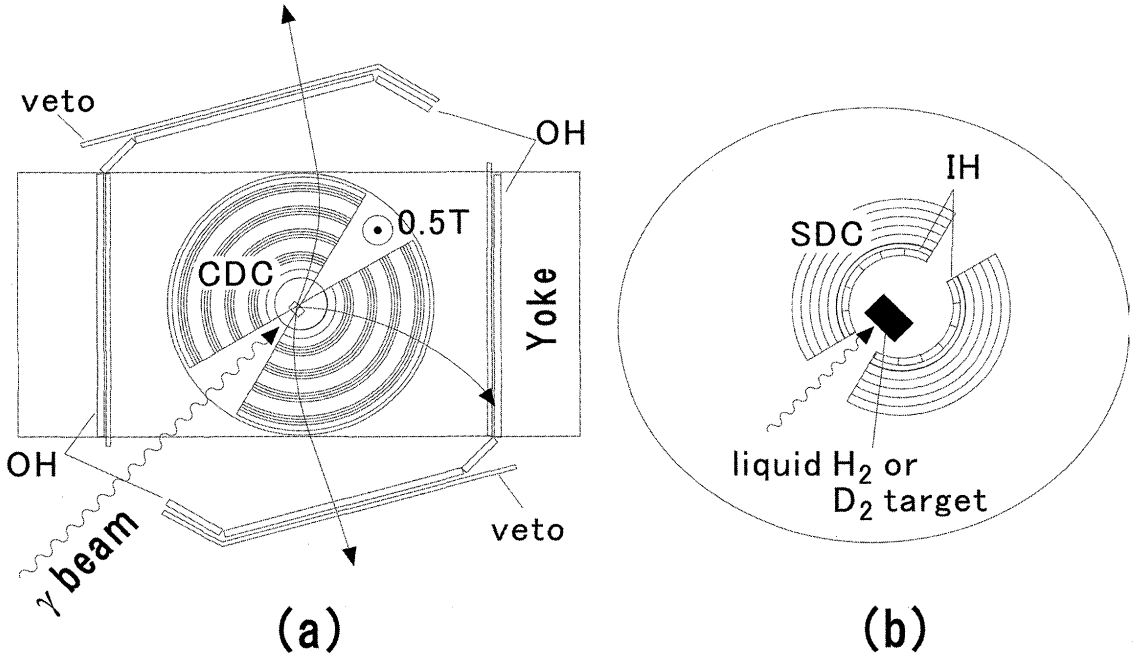

Fig.1. (a) Top view of the Neutral Kaon Spectrometer (NKS). It consists of a dipole magnet, hodoscopes (IH, OH), drift chambers (SDC, CDC) and veto counters. (b) Closeup of the center of the NKS. The target is located inside of the IH.

thickness. The hit position of the charged particle was determined by the time difference between two PMTs attached to the both ends of each scintillator. The typical TOF resolution was 0.5 ns.

2.3.3 Drift chambers

We employed two sets of drift chambers for the track and vertex reconstruction. Each set of the drift chamber consists of a straw type cylindrical drift chamber (SDC) and a honeycomb type one (CDC). They were located just around the IHs (Fig. 1). They covered an angular range from 15° to 165°on the both sides of the beam line. Each SDC contains 78 gold-plated tungsten wires of 20 μm ϕ for drift-time readout. The straws made of 180-μm thick aluminized Mylar film were used for field shaping. Each CDC contains 402 gold-plated tungsten wires of 30 μm ϕ for drift-time readout and 1094 molybdenum wires of 100 μm ϕ for field shaping. All wires were strung vertically and arranged in 16 concentric layers. Mixture of 50% Ar and 50% C_2H_6 was used for the drift gas.

2.3.4 Veto counters

In order to reduce the e^+e^- background along the beam line, the electron veto counters (EV) were employed. Each was made of a plastic scintillator of 1050 to 1250-mm length, 50-mm width and 5-mm thickness. The EVs were placed at the mid plane of the NKS magnetic field.

2.4 Data acquisition

The trigger condition required that there were at least two charged particles detected in coincidence on opposite sides of the beam line. The coincident signal of the left-, right-arm triggers and of the tagger signal was used as the trigger signal,

$$[\mathrm{TRIGGER}] = ([\mathrm{TAG}]\otimes[\mathrm{IH}])\otimes[\mathrm{LEFT}]\otimes[\mathrm{RIGHT}]\otimes\overline{[\mathrm{VETO}]}. \quad (3)$$

The [TAG] is the sum signal of tagging counters, and [IH] is the coincident signal between left- and right-side IH. The [LEFT] is the left-arm trigger defined as a coincident signal of left-side IH and OH without any hit of the EV. The trigger serves as the gate signal for ADCs and as the start signal for TDCs. Signals of the tagger, IH, OH and the EV were converted using the TKO modules. The CAMAC TDCs were used for drift chamber signals.

§3. Data analysis

3.1 Particle identification

The trajectory of a charged particle reconstructed by the SDC + CDC drift chamber system determines the horizontal momentum p_h and horizontal flight length l_h. A spline-fit method was employed for the reconstruction [14]. The time difference between two signals from the PMTs attached to the top and bottom of the OH gives the vertical flight length l_v. The TOF t is given from the time difference between the IH and OH signals. The velocity β and the momentum of the charged particle p

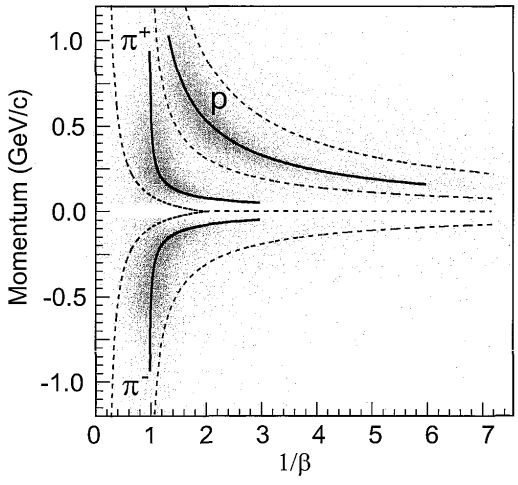

Fig.2. The β^{-1} vs. momentum of charged particles. Negatively charged particles are located in the negative signed momentum region.

are calculated by

$$\beta = \frac{\sqrt{l^2_h + l^2_v}}{ct}, \quad p = p_h \sqrt{1 - \left(\frac{l_v}{l_h}\right)^2}. \tag{4}$$

The particle mass is given by

$$m = \sqrt{\left(\frac{p}{c}\right)^2 \left(\frac{1}{\beta^2} - 1\right)} \ . \tag{5}$$

Figure 2 shows an example of the two-dimensional plot, where the abscissa and ordinate mean the β^{-1} and momentum, respectively. Solid lines indicate the masses of protons and charged pions. The proton contamination in the π^+ region and the π^+ contamination in the proton region are estimated to be less than 1.4% and less than 0.8%, respectively.

3.2 Vertex distribution

The vertex for the two-track events (V^{2track}) is defined as a point at which the distance between two tracks becomes minimum. Three V^{2track}s are found in the three-track events. As shown in Fig.3 (a), we

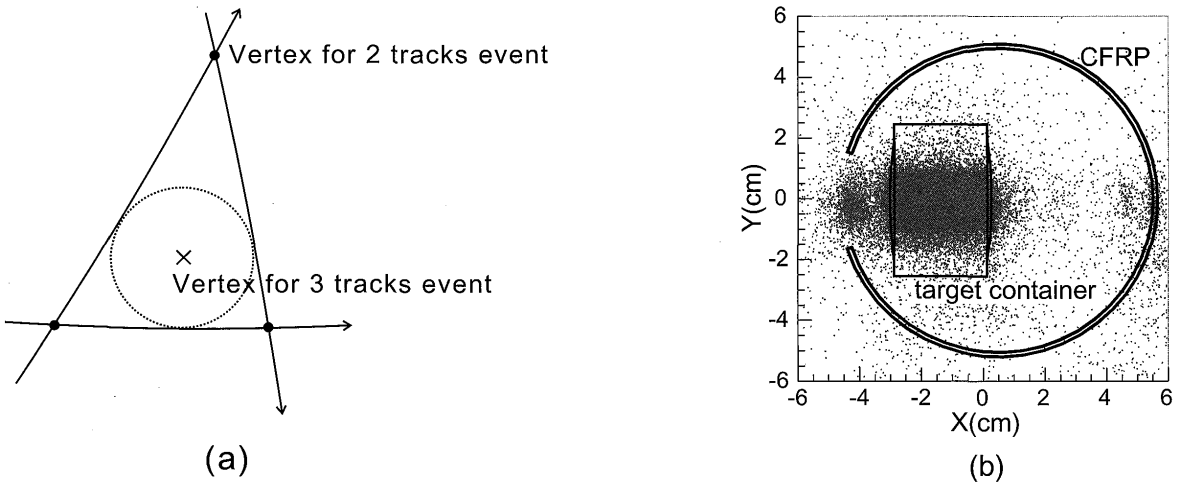

Fig.3. (a) A schematic drawing of the vertex definition for the three-track events. (b) The vertex distribution of three-track events.

determined the vertex for the three-track events V^{3track} as the center of the inscribed circle in the triangle constructed by three V^{2track}s. Figure 3 (b) shows the top view of the V^{3track} distribution. The solid lines indicate the position of the target container and the CFRP vacuum chamber.

3.3 Missing mass distribution

The missing mass for the $d(\gamma, p\pi^+\pi^-)X$,

$$M_X c^2 = \sqrt{\{(E_\gamma + M_d c^2) - (E_p + E_{\pi^+} + E_{\pi^-})\}^2 - c^2\{(p_\gamma + p_{\pi^+} + p_{\pi^-})\}^2}. \tag{6}$$

is shown in Fig.4 (a). The peak corresponding to the neutron mass is selected as the $d(\gamma, p\pi^+\pi^-)n$. The tail in higher energy side is supposed to be from 3π productions. The contamination of this background is estimated to be less than 4%

The M_X distribution for the $d(\gamma, p\pi^-)X$ is shown in Fig.4(b). The peak at a nucleon mass corresponds to the $d(\gamma, p\pi^-)p$. The peak at higher energy side is supposed to be double-, triple-pion productions. In order to reduce them, we imposed cuts on the opening angle between p and π^-, $\cos x_{p\pi} < 0.2$, and the angle of the $p\pi^-$ system, $\theta_{p\pi^-} < 10°$. This cut condition favors the quasi-free (QF) kinematics. The curves are the result of two-Gaussian fitting. We selected $Mx < 1.1$ GeV/c^2 as the "n"$(\gamma, p\pi^-)$. the "n" denotes

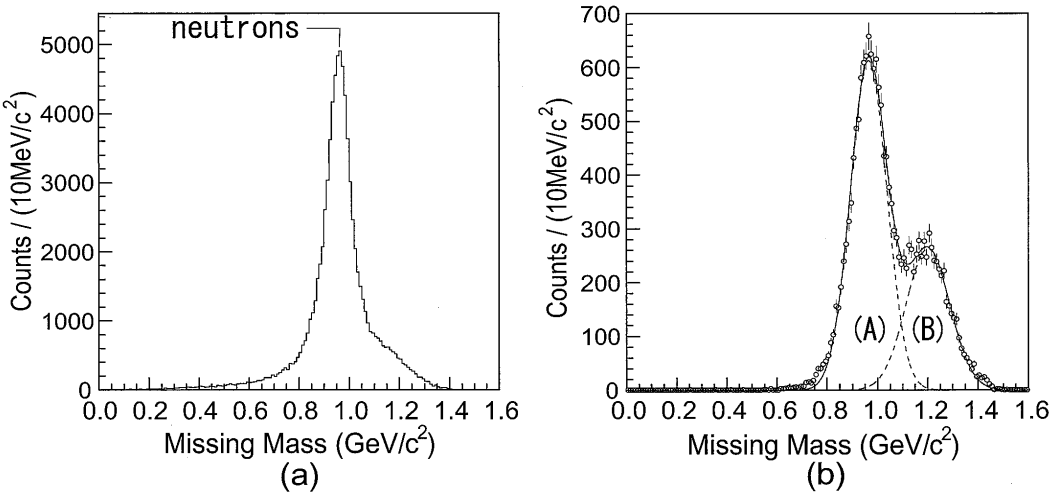

Fig.4. (a) The missing mass distribution for the $d(\gamma, p\pi^+\pi^-)X$. The peak corresponding to the neutron mass is selected as the $d(\gamma, p\pi^+\pi^-)n$. (b) The missing mass distribution for the $d(\gamma, p\pi^-)X$. It consists of two peaks as shown by dashed lines. The peak (A) is from $d(\gamma, p\pi^-)p$, and the peak (B) is thought to be from multi-pion productions.

the bound neutron in the deuteron. The contamination of the multi-pion background is estimated to be 2 ~ 15% in the entire photon energy range.

3.4 Invariant mass distribution

The invariant mass distributions for $N\pi$ and $\pi^+\pi^-$ pair in the $\gamma p \rightarrow p\pi^+\pi^-$ reaction are shown in Fig.5. Curves are the fitting results of Monte Carlo simulations described later. As reported in Refs. [1] and [15], the $\Delta^{++}\pi^-$ channel has a large contribution in this energy region. The peak around 1.35 GeV/c^2 in the $p\pi^-$ invariant mass corresponds to the $\Delta^{++}\pi^-$ channel, and the bump structure around 1.2 GeV/c^2 is thought to be the Δ^-.

The neutron momentum distribution for the $d(\gamma, p\pi^+\pi^-)n$ obtained from the missing momentum is shown in Fig.6. The solid curve corresponding to the nucleon momentum in the deuteron is derived by the simulation using Hulthén wave function [16]. The peak shifts toward higher momentum compared to Hulthen wave function because of the momentum resolution of the detected particles. If the

$p\pi^+\pi^-$ final state is produced through the QF kinematics with a neutron spectator, the neutron momentum (p_n) distribution should correspond to this curve. We selected $p_n < 0.2$ GeV/c as the "p"(γ, $p\pi^+\pi^-$). The "p" denotes the bound proton in the deuteron. It should be noted that the QF process with a proton spectator is also possible. But the momentum threshold of the NKS, about 0.25 GeV/c for protons, precludes the detection of these events almost entirely. We selected $p_n > 0.3$ GeV/c as the non quasi-free (NQF) kinematics in the $d(\gamma, p\pi^+\pi^-)n$.

The $N\pi$ invariant masses for the γ"p" $\rightarrow p\pi^+\pi^-$ reaction are shown in Fig.7. They are similar to those

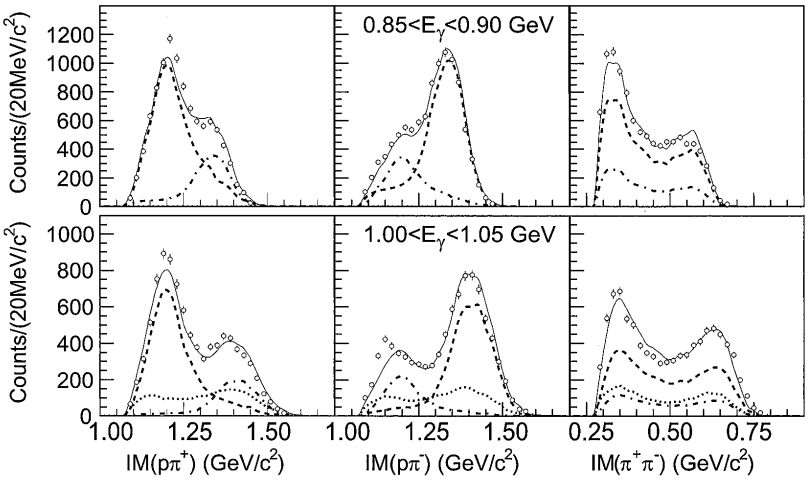

Fig.5. Invariant masses for the $\gamma p \rightarrow p\pi^+\pi^-$ reaction at two photon energies. The $\Delta^{++}\pi^-$ channel has a large contribution in this energy region. Curves show results of Monte Carlo simulations (see text). The dashed, dot-dashed and dotted curves represent the invariant masses for the $\Delta^{++}\pi^-$, $\Delta^0\pi^+$ channel and the three-body-phase-space simulation, respectively. The solid curves are the sums of them.

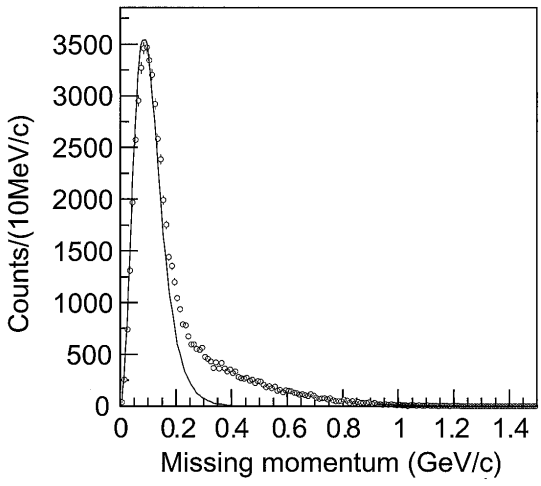

Fig.6. The neutron momentum distribution for the $d(\gamma, p\pi^+\pi^-)n$. The solid curve indicates the momentum distribution of the nucleon in the deuteron.

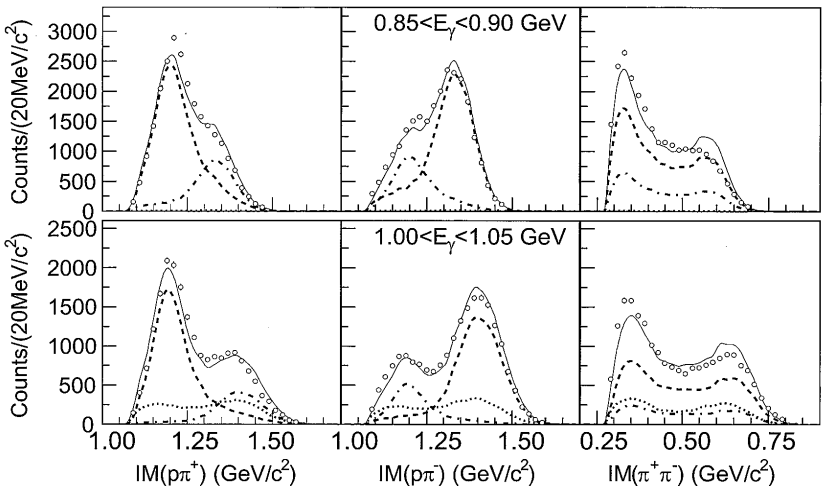

Fig.7. Invariant masses for the γ "p"$\rightarrow p\pi^+\pi^-$ reaction at two photon energies. Curves show results of Monte Carlo simulations (see text). The dashed, dot-dashed and dotted curves represent the invariant masses for the $\Delta^{++}\pi^-$, $\Delta^0\pi^+$ channel and the three-body-phase-space simulation, respectively. The solid curves are the sums of them.

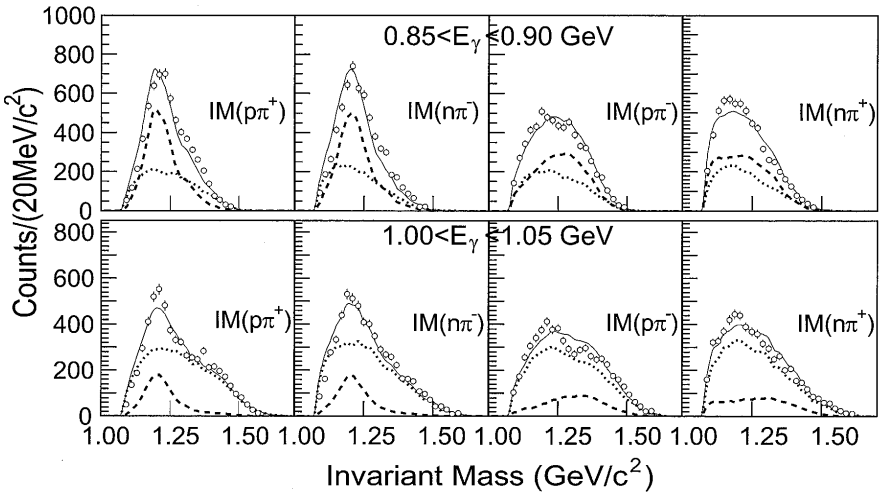

Fig.8. Invariant masses for the NQF process in the $d(\gamma, p\pi^+\pi^-)n$ at two photon energies. In this case, the peak of the Δ^- also appears. Curves show results of Monte Carlo simulations (see text). The dashed and dotted curves represent the invariant masses for the $\Delta^{++}\Delta^-$ channel and the four-body-phase-space simulation, respectively. The solid curves are the sums of them.

of the $\gamma p\rightarrow p\pi^+\pi^-$)n. reaction. Figure 8 shows the invariant masses in the NQF kinematics of the $d(\gamma, p\pi^+\pi^-)n$. Not only the peak of the Δ^{++} but also that of the Δ^- can be seen. A two-dimensional display of $p\pi^+$ and $n\pi^-$ invariant mass is shown in Fig.9. This figure suggests that there exists a large amount of the simultaneous excitation of two Δs.

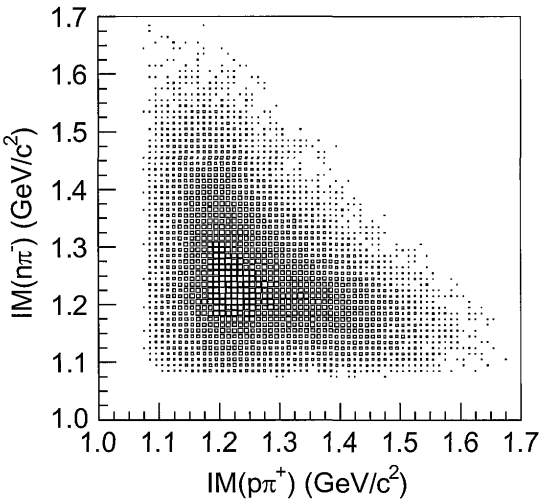

Fig.9. A two-dimensional display of $p\pi^+$ and $n\pi^-$ invariant mass.

3.5 Simulation

We have done Monte Carlo simulations, incorporating the geometry of the present experiment, in order to calculate the NKS acceptance and to separate each channel. The simulation outputs are transformed into the same format and analyzed in the same way as the experimental data.

We consider the $\Delta^{++}\pi^-$, $\Delta^0\pi^+$ channel and the three-body-phase-space as the channels in the $\gamma p \rightarrow p\pi^+\pi^-$ and γ"p" $\rightarrow p\pi^+\pi^-$ reaction. The angular distributions of the Δ^{++} were taken from Ref. [1]. We assume an isotropic angular distribution for the p and π^+ in the rest frame of the Δ^{++}. The $\Delta^0\pi^+$ was treated in the same manner as the $\Delta^{++}\pi^-$ described above. For the NQF in the $d(\gamma, p\pi^+\pi^-)n$, the $\Delta^+\Delta^-$ channel and the four-body-phase-space were taken into account. The $\Delta^+\Delta^0$ channel should also contribute. The Clebsh-Gordan coefficients lead to the following probability ratio of

$$\frac{\sigma(\Delta^{++}\Delta^- \rightarrow pn\pi^+\pi^-)}{\sigma(\Delta^+\Delta^0 \rightarrow pn\pi^+\pi^-)} = 9. \tag{7}$$

The most parts of the $\Delta^+\Delta^0$-decay contain at least one neutral pion. We exclude this channel, because it is invisible in the present experiment.

The sum of the simulated invariant masses were fitted to the experimental data. The curves in Figs. 5, 7 and 8 represent the results of this invariant mass fitting. The fractions of each channel were derived from this fitting. For example, the fraction of the $\Delta^{++}\Delta^-$ channel in the $\gamma p \rightarrow p\pi^+\pi^-$ reaction is given by

$$r_{\Delta^{++}\pi^-} = \frac{Y^{\mathrm{sim}}{}_{\Delta^{++}\Delta^-}}{Y^{\mathrm{sim}}{}_{\Delta^{++}\Delta^-} + Y^{\mathrm{sim}}{}_{\Delta^0\Delta^-} + Y^{\mathrm{sim}}{}_{3\mathrm{BPS}}}, \tag{8}$$

where the Y^{sim} is the fitted yield of each channel. The subscript 3BPS means the three-body-phase-space. We can obtain the experimental yield of the $\Delta^{++}\pi^-$ channel by

$$Y_{\Delta^{++}\pi^-} = Y_{p\pi^+\pi^-} r_{\Delta^{++}\pi^-}, \tag{9}$$

where the $Y_{p\pi^+\pi^-}$ is the experimental yield of the $\gamma p \rightarrow p\pi^+\pi^-$ reaction.

§4. Results and Discussion

The cross section for the i-th channel is calculated by

$$\sigma_i = \frac{Y r_i}{N_T N_\gamma \ \varepsilon_{DAQ} \ \varepsilon_{DC} \ \varepsilon^n_{track} \ \eta_i}, \tag{10}$$

where N_T is the number of the target atoms per unit area, N_γ is the number of the incident photons, Y is the total yield, r_i is the fraction of the i-th channel which is obtained by the invariant mass fitting, ε_{DAQ} is the data-acquisition efficiency, ε_{DC} is the selection efficiency of track candidates, and ε^n_{track} is the tracking efficiency. The number of the reconstructed tracks is n. The acceptance correction factor of the i-th channel η_i is obtained by the simulation and given as the ratio of the number of accepted events to that of the generated ones. The total cross section is given as the sum of the partial cross sections,

$$\sigma_{tot} = \Sigma \sigma_i . \tag{11}$$

The σ_{tot} for the $\gamma "n" \rightarrow p\pi^-$ reaction is shown in Fig.10. The error bars represent the statistical uncertainties. The results of previous works of Refs. [17-19] are also shown for comparison.

The total cross sections for the $\gamma p \rightarrow p\pi^+\pi^-$ and $\gamma p \rightarrow \Delta^{++}\pi^-$ reaction are shown in Fig.11 (a) and (b),

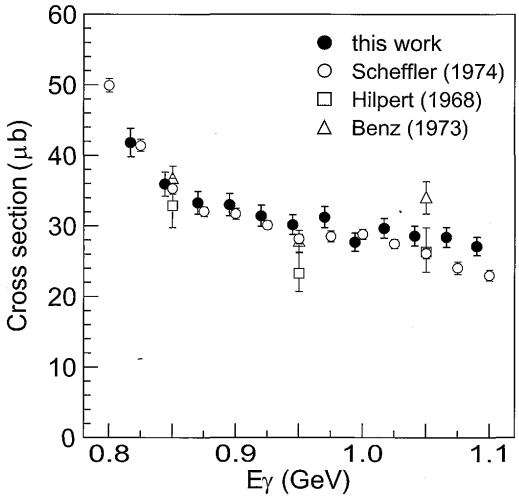

Fig.10. The σ_{tot} for the $\gamma d \rightarrow pp\pi^-$. The filled circles show the results of this work. The open circles, squares and triangles represent the results of Sheffler *et al.* [17], Hilpert *et al.* [18] and Benz *et al.* [19].

respectively. The error bars represent the statistical uncertainties. The results of previous works of ABBHHM [1] and SAPHIR [15] are also shown for comparison. Our results show good agreement with them.

The σ_{tot} for the $\gamma "p" \rightarrow p\pi^+\pi^-$ reaction is shown in Fig.12 (a). The error bars represent the statistical uncertainties. The results of previous works of Refs. [3, 4, 10] are also shown for comparison. The data of Refs. [3, 4] were measured using deuteron bubble chambers, while those of Ref. [10] were measured using a magnetic spectrometer. From the results of Refs. [4, 10] , the cross section values are about 75 μb around E_γ = 0.8 GeV. They are close to that of the $\gamma p \rightarrow p\pi^+\pi^-$ reaction. But from our results, it turned

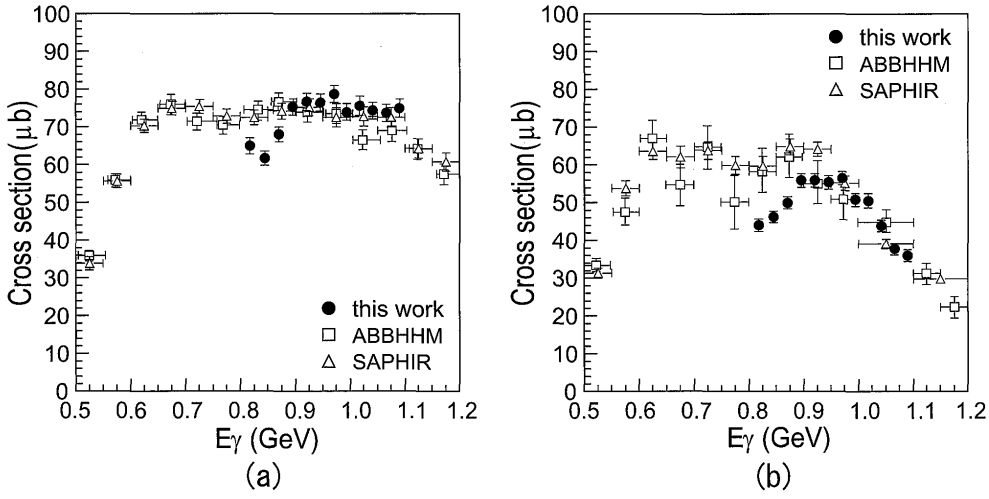

Fig.11. (a) The σ_{tot} for the $\gamma p \rightarrow p\pi^+\pi^-$. (b) The cross section for the $\gamma p \rightarrow \Delta^{++}\pi^-$. The filled circles show the results of this work. The open squares and triangles represent the results of ABBHHM [1] and SAPHIR [15].

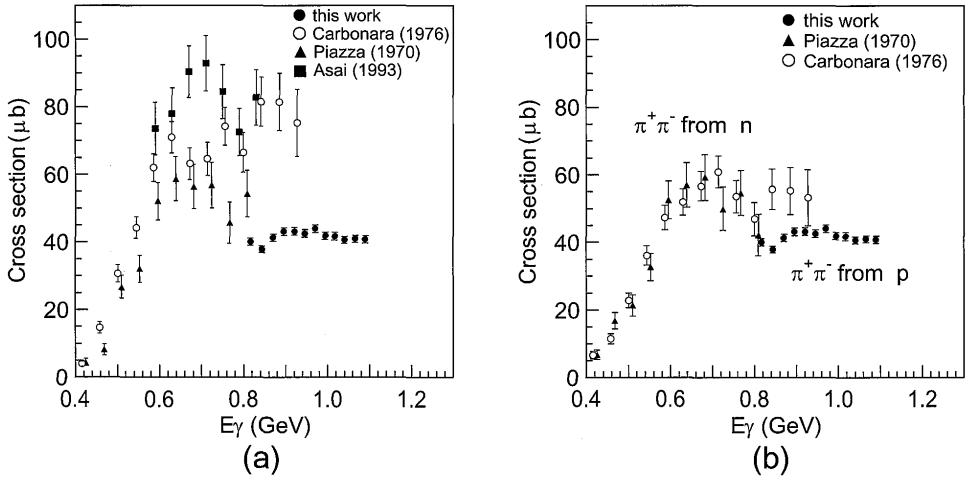

Fig.12. (a) The σ_{tot} for the $\gamma "p" \rightarrow p\pi^+\pi^-$. The filled circles show the results of this work. The filled triangles, open circles and filled squares represent the results of Piazza *et al.* [3]. Carbonara *et al.* [4] and Asai *et al.* [10] (b) Comparison with the $\gamma "n" \rightarrow n\pi^+\pi^-$. The filled circles show the results of this work for the $\gamma "p" \rightarrow p\pi^+\pi^-$, The filled triangles and open circles represent the results of Piazza *et al.* [3] . and Carbonara *et al.* [4] for the $\gamma "n" \rightarrow n\pi^+\pi^-$,

out that the cross section values were smaller than the previous results and were about 40 μb. Our results are in agreement with the results of Ref. [3] . In Fig. 12 (b), the σ_{tot} for the $\gamma"p" \rightarrow p\pi^+\pi^-$ reaction are compared with those for the $\gamma"n" \rightarrow n\pi^+\pi^-$ reaction. Filled triangles and open circles are taken from Refs. [3, 4], respectively. We conclude that the total cross section for the $\gamma"p" \rightarrow p\pi^+\pi^-$ reaction is roughly same as that for the $\gamma"n" \rightarrow n\pi^+\pi^-$ reaction. This seems to be consistent considering that the total photoabsorption cross section on the deuteron is about twice as large as that on the proton.

Figure 13 shows the cross section for the $\gamma d \rightarrow \Delta^{++}\Delta^-$ reaction. Filled circles show the results of this work. The statistical errors are smaller than the plot size. For comparison the results of previous works of Refs. [10, 20, 21] are also shown in this figure. Our results are smaller than others. But the errors of Refs.[10, 21] are very large. The results of this work shows the decreasing behavior with the photon energy.

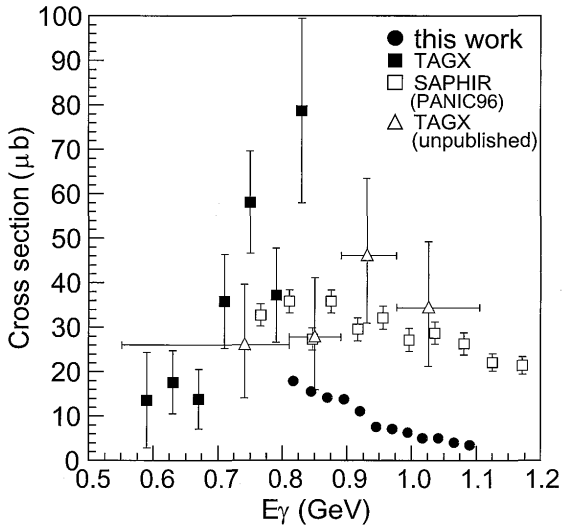

Fig.13. The cross section for the $\gamma d \rightarrow \Delta^{++}\pi^-$. The filled circles show the results of this work. The filled squares, open squares and open triangles represent the results of Asai *et al*, Wada *et al.* [20] and Shinozaki *et al.* [21].

The $\Delta^{++}\Delta^-$ production accounts for 4 % at E_γ= 0.8 GeV and 1% at E_γ= 1.1 GeV of the total photoabsorption cross section on the deuteron.

The cross section for the NQF process has almost no dependency on the photon energy as well as those of the QF process. The cross section ratio of the NQF to the QF process is found to be $\sigma_{NQF} / 2\,\sigma_{QF} \sim 0.3$.

§5. Summary and Conclusion

Total cross sections have been measured for the $p(\gamma, p\pi^+\pi^-)$, $"p"(\gamma, p\pi^+\pi^-)$ reaction and the non-quasi-free process of the $d(\gamma, p\pi^+\pi^-)n$ reaction in the energy range from 0.8 to 1.1 GeV. The total cross section for the $\gamma p \rightarrow p\pi^+\pi^-$ reaction shows good agreement with previous data. The quasi-free process was selected by applying the kinematical cut on the missing momentum. The total cross section for the $\gamma"p" \rightarrow p\pi^+\pi^-$ reaction was found to be 50 ~ 60% compared to that of the "free" proton.

The cross section for the $\gamma d \rightarrow \Delta^{++}\Delta^{-}$ reaction was measured. The magunitude is smaller than previous data and shows decreasing behaviour with the photon energy.

Acknowledgement

We thank the accelerator and technical stuff at LNS for their contributions to the succsess of the experiment.

References

[1] Aachen-Berlin-Bonn-Hamburg-Heidelberg-Munchen Collaboration: Phys. Rev. **175** (1968) 1669.

[2] Canbridge Bubble Chamber Group: Phys. Rev. **169** (1968) 1081.

[3] A. Piazza *et al.*: Nuovo Cimento **3** (1970) 403.

[4] Carbonara *et al.*: Nuovo Cimento **36A** (1976) 219.

[5] F.Härter *et al.*: Phys. Lett. **B40** (1997) 229.

[6] B. Krusche *et al.*: Eur. Phys. J. **A6** (1999) 309.

[7] T.A. Armstrong *et al.*: Phys. Rev. **D5** (1972) 1640.

[8] T.A. Armstrong *et al.*: Nucl. Phys. **B41** (1972) 445.

[9] M. MacCormic *et al.*: Phys. Rev. **C53** (1996) 41.

[10] M. Asai *et al.*: Z. Phys. **A344** (1993) 335.

[11] H. Yamazaki *et al.*: Nucl. Instr. and Meth. **A536** (2005) 70.

[12] *Ube Ultra-High Heat-Resistant Polyimide Film,* Ube Industries Ltd. (2000).

[13] Vector Fields Limited, Oxford, England.

[14] H. Wind : Nucl. Instr. and Meth. **115** (1974) 431.

[15] C. Wu *et al.*: Eur. Phys. J. **A23** (2005) 317.

[16] D.H. White, R.M. Schectman, and B.M.Chasan: Phys. Rev. **120** (1960) 614.

[17] P.E. Scheffler and P.L. Walden: Nucl. Phys. **B75** (1974) 125.

[18] H.G. Hilpert *et al.*: Nucl. Phys. **B8** (1968) 535.

[19] P. Benz *et al.*: Nucl. Phys. **B65** (1973) 158.

[20] Y. Wada, for the SAPHIR Collaboration: *Particles and nuclei international conference, Williamsburg, Virginia, 1996.*

[21] A. Shinozaki, for the TAGX Collaboration: *private communication.*